

Enhancing Resistance to Wetting Transition through the Concave Structures

Jinhoon Lee, Jinwoo Park, Kwang Hui Jung, Seunghyun Lee, Jeong Jun Lee, Sanghyuk Wooh, and Dong Woog Lee*

Water-repellent superhydrophobic surfaces are ubiquitous in nature. The fundamental understanding of bio/bio-inspired structures facilitates practical applications surmounting metastable superhydrophobicity. Typically, the hierarchical structure and/or reentrant morphology have been employed hitherto to suppress the Cassie-Baxter to Wenzel transition (CWT). Herein, a new design concept is reported, an effect of concave structure, which is vital for the stable superhydrophobic surface. The thermodynamic and kinetic stabilities of the concave pillars are evaluated by continuous exposure to various hydrostatic pressures and sudden impacts of water droplets with various Weber numbers (We), comparing them to the standard superhydrophobic normal pillars. Specifically, the concave pillar exhibits reinforced impact resistance preventing CWT below a critical We of ≈ 27.6 , which is ≈ 1.6 times higher than that of the normal pillar (≈ 17.0). Subsequently, the stability of underwater air film (plastron) is investigated at various hydrostatic pressures. The results show that convex air caps formed at the concave cavities generate downward Laplace pressure opposing the exerted hydrostatic pressure between the pillars, thus impeding the hydrostatic pressure-dependent underwater air diffusion. Hence, the effects of trapped air caps contributing to the stable Cassie-Baxter state can offer a pioneering strategy for the exploration and utilization of superhydrophobic surfaces.

1. Introduction

The wetting of liquids on solid surfaces illustrates contacting droplets on the surfaces with a specific contact angle and that can be expressed as a balance between surface tensions at interfaces.^[1] The rough topology of the surface further suggested the Wenzel model and the Cassie-Baxter model,^[2] which elucidates the correlation between surface topology and wettability. Specifically, the water-repellent superhydrophobic surface has been accomplished by the combination of a rough surface and low surface energy, hanging vapor/liquid interfaces between their protrusions,^[3] which is known as the Cassie-Baxter state. Utilizing the peculiar properties of water repellency from superhydrophobic surfaces, recently, applications for self-cleaning,^[4] anti-icing,^[5] droplet manipulation,^[6] anti-fouling,^[7] catalysis,^[8] and energy harvesting^[9] have attracted attention. However, the utilization of superhydrophobic surfaces for practical engineering applications is restricted due to their metastable performances.^[10] Thus, unveiling and enhancing the stability and

durability of superhydrophobicity under harsh conditions are of great concern.^[11]

In nature, several species live in terrestrial and marine environments, thereby evolving themselves to possess peculiar surface features and structures concerning their diverse ecosystems.^[12] Their exclusive surface morphologies have guided an extreme water repellency such as stable air entrapment underwater^[13] and bouncing high-impact pressure of raindrops,^[14] preventing the Cassie-Baxter to the Wenzel transition (CWT). Therefore, they have signposted a biomimetic approach as a blueprint for fabricating artificial superhydrophobic surfaces.^[15] Representatively, the multiscale nano-microhierarchical structure,^[16] closed pore structure,^[17] and mushroom-like reentrant structure^[17a,18] have been employed to implement wetting stability. Those unique structures have offered design concepts for artificial superhydrophobic surfaces and contributed to revealing the fundamental mechanism for a stable Cassie-Baxter state. Arising from that, factors like energy barrier,^[19] capillary pressure,^[20] line energy on the nanostructure,^[14c,21] and air compressibility^[17b,22] are considered

J. Lee, J. Park, K. H. Jung, S. Lee, D. W. Lee
Ulsan National Institute of Science and Technology
50 UNIST-gil, Ulsu-gun, Ulsan 44919, Republic of Korea
E-mail: dongwoog.lee@unist.ac.kr

J. J. Lee
School of Life Sciences
Seoul National University
1 Gwanak-ro, Gwanak-gu, Seoul 08826, Republic of Korea
S. Wooh
Department of Chemical Engineering
Chung-Ang University
84 Heukseok-ro, Dongjak-gu, Seoul 06794, Republic of Korea

 The ORCID identification number(s) for the author(s) of this article can be found under <https://doi.org/10.1002/adma.202409389>

© 2024 The Author(s). Advanced Materials published by Wiley-VCH GmbH. This is an open access article under the terms of the [Creative Commons Attribution-NonCommercial](#) License, which permits use, distribution and reproduction in any medium, provided the original work is properly cited and is not used for commercial purposes.

DOI: 10.1002/adma.202409389

crucial for designing stable superhydrophobic surfaces. Likewise, the research on bio/bioinspired surfaces has addressed both the in-depth exploration and practical applications for state-of-the-art superhydrophobic surfaces.

In this work, we report the effect of trapped air on the stable superhydrophobicity induced by a concave pillar (CP) structure which is found in the pulvilli of some leaf beetle species and the soil-dwelling springtail (collembola) species.^[23] It is important to note that the CP is an open pore structure without reentrancy and hierarchy, solely accounting for the concave effect (air-trapping on the concave structure) on the wetting stability. To investigate the contribution of solid or line fraction at the air/water interfaces, CP surfaces with fixed pillar diameter (D) and various pillar-to-pillar lengths (L) are fabricated. Initially, the dynamic wettability of CP surfaces during the impact is evaluated by comparing them to conventional superhydrophobic surfaces with cylindrical normal pillar (NP) structures with the same D/L . Unlike the NP surfaces, notably the CP surface with the highest line fraction, $D/L = 0.5$, shows a significant increase in both the impact and hydrostatic pressure stability. Our findings of transition-resistant CP structure provide the pioneering design concept as to feasible superhydrophobic surfaces with the stable Cassie-Baxter state for exploration and state-of-the-art applications.

2. Result and Discussion

2.1. Fabrication of Superhydrophobic Concave Pillar Microstructures

The design of CP surfaces was inspired by a concave morphology in nature such as pulvilli on the feet of leaf beetles (Figure 1a–c) and the cuticles from various springtail species.^[23b,c] In the requirements of self-cleaning to prevent contamination on their adhesive parts, insects normally possess rough structures with superhydrophobic properties on their feet.^[24] Likewise, the pulvilli of the leaf beetles, especially for the male, possess an adhesive pad with a concave structure on their feet; and are considered to facilitate adhesion to the leaves and the roughly structured elytra of the female during the copulation (Figure 1a).^[23c] On the other hand, the soil-dwelling springtail species are believed to have the nano/microstructure on their cuticles for respiration even in their harsh habitat environment. Keeping a stable air film is vital for respiration, thus the complex structures (including reentrancy and concavity) are considered to be critical for maintaining a stable air film on their cuticle in temporary rain flooding and humid soil habitats.^[23b] Therefore, we mimicked the concavity of such structures to investigate the contribution of the concavity to the wetting stability of superhydrophobic surfaces.

Figure 1d shows summarized schematics for the CP microstructure fabrication. The following top-down processes were conducted to fabricate the concave-shaped pillars on the surface. The photoresist (PR) was spin-coated on the SiO_2 surface and patterned into hexagonal circle arrays via photolithography. The SiO_2 layer was then vertically etched along the same hexagonal patterns of the PR film. The SiO_2 etching revealed the silicon surface underneath the patterned SiO_2 layer. We then employed potassium hydroxide (KOH) and isopropyl alcohol (IPA) for the

wet etching process to acquire an inverted pyramidal shape on the silicon surfaces. Within the KOH etching process, the (111) plane of silicon is etched more slowly than other planes, thus the inverted pyramidal shapes could be obtained (Figure S1, Supporting Information). Moreover, the addition of IPA improves the smoothness of the etched surface and decreases the etching rate, making a shallow bottom surface.^[25] Afterward, a 0.3 μm thickness of chromium (Cr) layer was deposited on the whole surface and the Cr layer on SiO_2 was lifted off simultaneously, etching the SiO_2 layer in buffered oxide etchant (BOE). The revealed silicon surface was vertically etched to get pillar-shaped microstructures (Table S1, Supporting Information),^[26] and then the wafer was immersed in Cr etchant to remove the Cr layer on concave parts. To get rid of nanograsses among the pillars, the surface was immersed in pure ethanol followed by gentle sonication. Removing the nanograsses rules out the effect from a hierarchical (multi-scale) structure.^[7b,16,22] Lastly, fluorosilanization was conducted after air plasma treatment for the superhydrophobic CP microstructures (Figure S2, Supporting Information). It is also important to note that the fabricated CP is neither a closed pore structure nor a reentrant structure which were previously considered as critical factors in enhancing wetting stability.^[17,18b] Therefore, by utilizing CP, we can focus solely on the effect of concave structures on wetting stability.

Figure 1e,f shows the manufactured CP surfaces identified with scanning electron microscopy (SEM) imaging before fluorosilanization. The fabricated concave pillar structures show a pillar diameter (D) of 20 μm , base diameter for concavity (b) of 10 μm , 20 μm of pillar height (H_p), and $\approx 54.5^\circ$ of etched angle exposing (111) plane of silicon (Figure S1b, Supporting Information). To verify the concave effect regarding line fraction at the air/water interfaces, 6 types of CP surface were fabricated with a fixed diameter of 20 μm and D/L of 0.083, 0.125, 0.17, 0.25, 0.33, and 0.5, respectively (Figure S3, Supporting Information). Except for the CP surface with $D/L = 0.083$, all the surfaces exhibited the Cassie-Baxter state with over 150° of water contact angle (apparent contact angle, θ_{apa}) and contact line shifting when measuring the dynamic contact angle (advancing contact angle, θ_{adv} , and receding contact angle, θ_{rec}) (Figure 1g). We also demonstrated the self-cleaning property of pillars with concavity using the CP surface of $D/L = 0.5$ (Figure S4, Supporting Information). Therefore, we carried out an in-depth evaluation with 5 different surfaces ($D/L = 0.125, 0.17, 0.25, 0.33$, and 0.5).

2.2. Droplet Dynamic Behaviors on the CP Surfaces

Several studies have demonstrated that the pressure-resistant properties of superhydrophobic surfaces resulted from several factors, for instance, capillary force of structure, line energy, and air compression.^[14c,17b,20a] As a result, the droplets falling on the superhydrophobic surface exhibit a series of dynamic behaviors: impacting, pancake-like spreading, retracting, and finally detaching. Here, the dynamic wettability on the CP surfaces was characterized using a high-speed camera, recording at the frame rate of 2500 fps. For the comparison, we also fabricated the typical superhydrophobic surfaces with cylindrical normal pillars (NP) which possess similar D and L of CP (Note S1 and Figures S5–S7, Supporting Information).

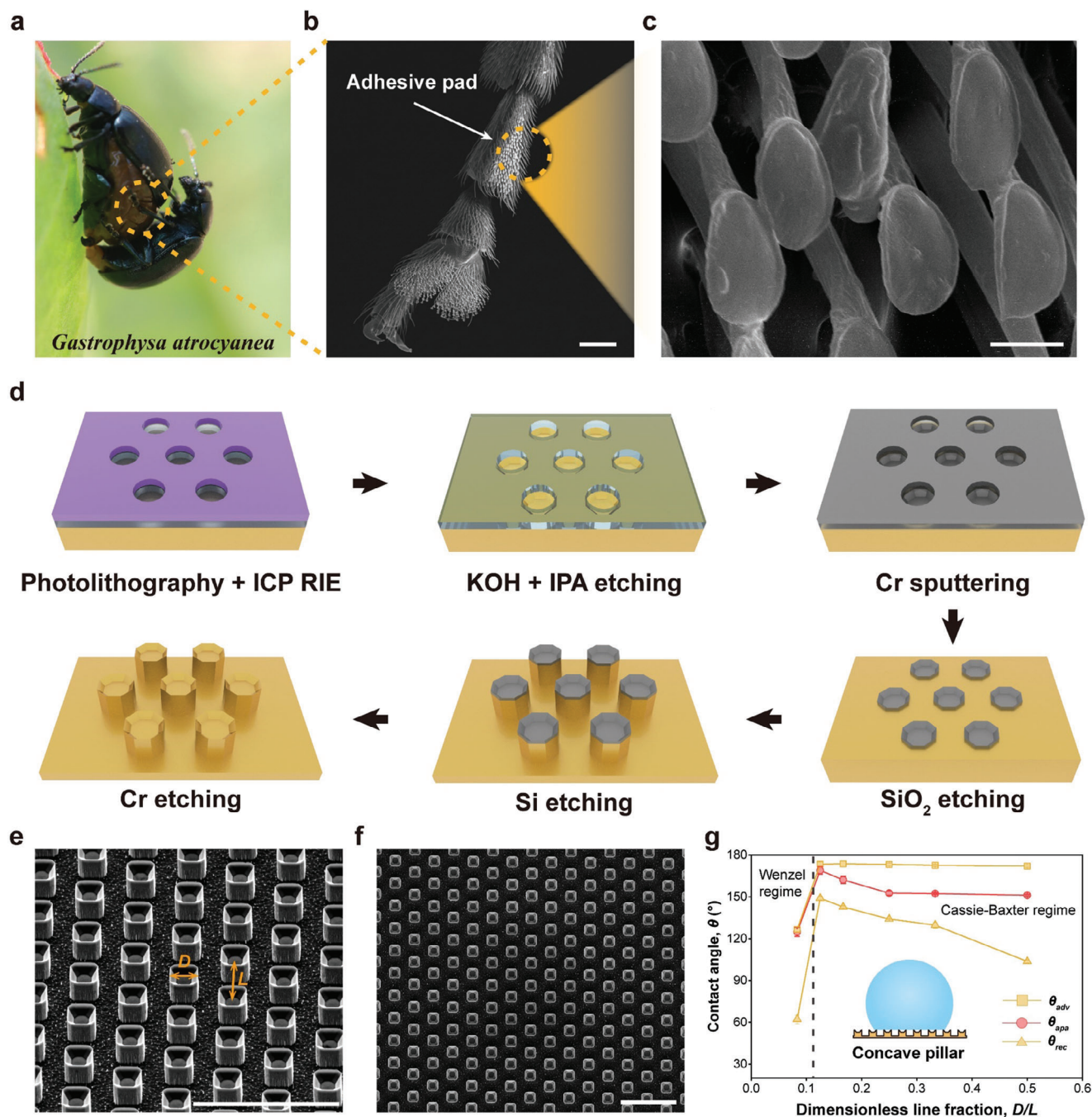


Figure 1. Inceptive design for concave pillar microstructure fabrication. a) Digital image of a leaf beetle, *Gastrophysa atrocyanea*, b) microscopic view of the leaf beetle feet, and c) pulvilli on the feet possessing a discoidal concave structure from the edge utilizing scanning electron microscopy. d) Brief schematics as to the overall fabrication process for the concave pillar. e, f) Representative scanning electron microscopy images of concave pillar structures with D and L of 20 and 40 μm , respectively. g) Static (θ_{apa}) and dynamic (θ_{adv} and θ_{rec}) water contact angle of the fabricated concave pillar surfaces. The scale bars denote 100 μm for b, e, and f; and 5 μm for c.

Figure 2 illustrates the dynamic behavior of water droplets on i) NP surfaces and ii) CP surfaces according to each D/L , utilizing the ultrapure deionized (DI) water (18.2 $\text{M}\Omega$ resistance). Water droplets of $\approx 2 \mu\text{L}$ (diameter of $\approx 1.56 \text{ mm}$, less than the capillary length of 2.7 mm) were dropped at various heights. We then focused on the dynamic behavior at the terminal impact velocity, v_t ,

when the NP surfaces allowed the CWT (the determination of v_t is in the Experimental section).

The dimensionless contact diameter was traced in terms of contacting length/initial droplet diameter, l_c/d_0 (see inset of Figure 2a), as a function of time after collision (t_c). Concurrently, the determination of (partial) CWT or stable Cassie-Baxter

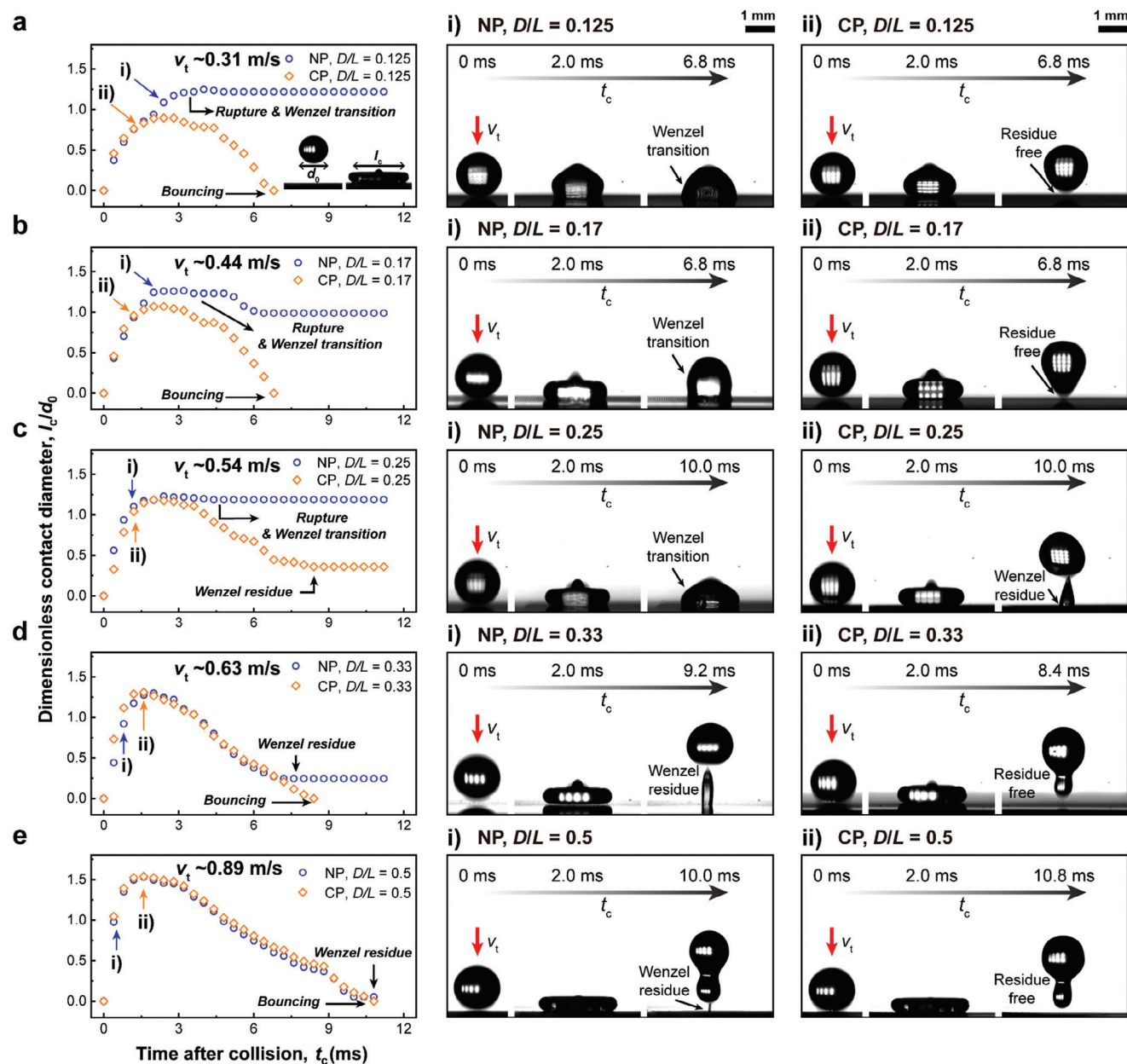


Figure 2. Dynamic behavior of water droplets on the NP and CP surfaces with varying D/L . Plots showing dimensionless contact diameter (contacting length (l_c)/initial droplet diameter (d_0)) and snapshots of bouncing droplets as a function of time after collision (t_c) on i) NP surface and ii) CP surface with a) $D/L = 0.125$, b) $D/L = 0.17$, c) $D/L = 0.25$, d) $D/L = 0.33$, and e) $D/L = 0.5$.

state (manifested by the bouncing of droplets without droplet residues) was screened (bouncing on the NP surfaces is depicted in Figure S8 and Movie S1, Supporting Information). Specifically, the partial CWT was largely determined by two points, a necking of the droplet (cohesion failure) and the smaller contact angle (than the θ_{rec} in Figure 1g; and Figure S7, Supporting Information) during retraction.^[14c,27] The CP surfaces ($D/L = 0.125$, 0.17) completely rebounded the droplets ($v_t \approx 0.31$, ≈ 0.44 m s⁻¹, respectively); however, the NP surfaces ($D/L = 0.125$, 0.17) exhibited the complete CWT without retraction (Figure 2a,b; and

Movie S2, Supporting Information). Additionally, the NP surface of $D/L = 0.25$ also resulted in the complete CWT at the velocity of ≈ 0.54 m s⁻¹ but, only the partial CWT was observed for the CP surface leaving behind the Wenzel residue (Figure 2c; and Movie S2, Supporting Information). CP surfaces with the higher D/L of 0.33 and 0.5 performed complete bouncing at $v_t \approx 0.63$ and ≈ 0.89 m s⁻¹ while the NP surfaces exhibited partial CWT (Figure 2d,e; and Movie S2, Supporting Information). The concave effect enhanced the impact resistance along the various surfaces regardless of line fractions.

2.3. Impact Pressure Stability of CP Surfaces

While we have provided the enhanced impact pressure resistance of CP surfaces originating from the concave effects, the question was when the CP surfaces would allow the invasion of water droplets through the air/water interfaces. As for the identification, we further evaluated the pressure stability of CP surfaces in detail at higher falling heights, comparing them to the NP surfaces (Figure S9 and Movie S3, Supporting Information). Weber number We , where $We = \frac{\rho v_t^2 d_0}{\gamma}$, ρ is the density and γ is the surface tension of water ($\approx 1000 \text{ kg m}^{-3}$ and $\approx 72 \text{ mN m}^{-1}$, respectively), is a key parameter for the investigation of droplet dynamic behavior, involving the energy state of a droplet. Thus, we explored the CWT regime for both NP and CP surfaces based on We . The detailed impact dynamics on the surfaces were investigated under the aforementioned method using $\approx 2 \text{ }\mu\text{L}$ of water droplets with increasing the heights by the step of 0.5 cm . In this experiment, 0.5 cm higher height corresponds to an increased We by ≈ 2.1 .

Figure 3a shows the wetting phase map of the NP and CP surfaces depending on the D/L and We . Generally, surfaces with lower D/L , and/or droplets with higher We tend to induce partial CWT and complete CWT. Surprisingly, the CP surface with the highest $D/L \approx 0.5$ completely rebounded the droplet with $We \approx 25.5$ and showed a partial CWT at a critical $We \approx 27.6$. This critical We is ≈ 1.6 times higher compared to that of NP surface (≈ 17.0). Even though the effect from the concavity was relatively less than the $D/L \approx 0.5$ surfaces, other CP surfaces ($D/L = 0.125$ – 0.33) also exhibited better impact pressure-resistant properties than the NP surfaces (Figure 3a).

Mainly, the transition to the Wenzel state during droplet impact has been considered as a depinning of the air/water interfaces and a sagging of the interfaces due to inertia (Figure 3b).^[20b] The CWT of the CP surfaces with $D/L = 0.5$ and different aspect ratios (D/H_p) also supports the depinning/sagging of the interfaces during the droplet impact. The CP surface of $D/H_p \approx 1.8$ showed the partial CWT at a slightly smaller critical $We \approx 23.4$ (Figure S10, Supporting Information), but still higher than the NP (critical $We \approx 17.0$). Whereas the CP surfaces with $D/H_p \leq 1$ experienced a partial CWT at an equal critical We of ≈ 27.6 (Figure S11, Supporting Information). These results indicate that the $D/H_p = 1$ ($H_p = 20 \text{ }\mu\text{m}$) seems to be enough to protect the air/water interface touch the bottom of the microstructures during instantaneous sagging of the interfaces due to the inertia.

When the droplets contact the solid surfaces instantaneously, henceforth, there could be a water hammer pressure (P_H) and a dynamic pressure (P_D) striking the surfaces and facilitating CWT on the surfaces.^[14c,20c,22,28] To prevent penetration of water droplets into the structures, the capillary pressure (P_C) should be higher than the impacting pressure. As P_C is enhanced by an increase in D/L , commonly the higher line fraction of the surface results in more stable pressure resistance against impacting pressure (detailed calculations of P_C are depicted in Note S2 and Figure S12, Supporting Information). The impact pressure P_H and P_D are described as $P_H = k_{wh} \rho C v_t$, $P_D = 0.5 \rho v_t^2$, respectively, where k_{wh} is a water hammer coefficient and C is sound speed in water (1497 m s^{-1}).^[20c] As for previous studies, the impact pres-

sure could be balanced with the P_C then, the k_{wh} is expressed as:^[20c]

$$k_{wh} = \frac{P_C - P_D}{\rho C v_t} \quad (1)$$

In particular, the k_{wh} had been considered as the value of 0.2 ,^[27] but several studies have experimentally revealed that the coefficient should be decreased by at least two orders of magnitude for the superhydrophobic microstructures,^[28] presenting a linear relationship with P_C .^[20c,22] The v_t in Equation 1 refers to the critical impact velocity at which the surface confronts partial CWT (further discussion is in Note S3, Supporting Information).

We then analyzed the relationship between the experimental parameter k_{wh} and P_C for both NP and CP surfaces. The NP surfaces show a linear correlation between k_{wh} and P_C in line with previous studies (Figure S13 and Table S2, Supporting Information).^[20c,22] To support the linear relationship between P_C and k_{wh} , we additionally fabricated a truncated cone pillar (TCP) surface with $D/L = 0.5$ (Note S4, Figure S14, and Table S3, Supporting Information), which could exhibit multiple capillary pressures. The fabricated TCP surface also shows a stable Cassie-Baxter state (Note S5 and Figure S15, Supporting Information). TCP surface is expected to contain no air caps, which resulted in a significantly smaller critical $We \approx 22.3$ compared to that of CP (≈ 27.6). Interestingly, TCP still exhibited higher CWT resistance compared to the NP (critical $We \approx 17.0$), which may be due to the presence of multiple capillary pressures (further discussions in Note S5, Figure S16, and Movie S4, Supporting Information).

The k_{wh} values of the CP surfaces with $D/L < 0.5$ are similar to NP, also showing a linear relationship. However, the CP surface with $D/L = 0.5$ shows a k_{wh} value of ≈ 0.00109 , smaller than what is expected from the linear relationship. As for the discussion in previous studies, the closed cavity surfaces, which exhibit air spring effect, accomplished high impact pressure resistance compared to the open pillar structures.^[17b] Judging from that, the kinetic energy of the impacting droplet to our CP surface ($D/L = 0.5$) could be compensated by the compressed air on the concave parts resulting in the prevention of the water penetration through air/water interfaces between pillars. These comprehensive results allowed us to speculate that the outstanding pressure stability of the CP surface ($D/L = 0.5$) strongly depends on the air compression-induced air spring effect rather than P_C . In other words, a higher line fraction of 0.5 or more is essential for a potent concave effect on enhancing the impact pressure resistance.

We also fabricated the CP surface with $D/L = 0.56$ through the further 5 min of KOH + IPA wet etching process to verify whether the line fraction of 0.5 or more is effective for the impact pressure resistance or not (Figure S17a,b, Supporting Information). Indeed, the CP surface ($D/L = 0.56$) underwent the partial CWT at a critical We of ≈ 38.2 (critical velocity of $\approx 1.33 \text{ m s}^{-1}$) (Figure S17c,d, and Movie S5, Supporting Information), where ≈ 1.4 times higher critical We than the CP surface of $D/L = 0.5$ (≈ 27.6). Meanwhile, CP surfaces with D/L higher than 0.56 cannot be fabricated without defects due to the saturation of the etching rate during the KOH + IPA etching process.

Owing to the air spring effect from trapped air seems to strongly contribute to the impact pressure resistance of the CP

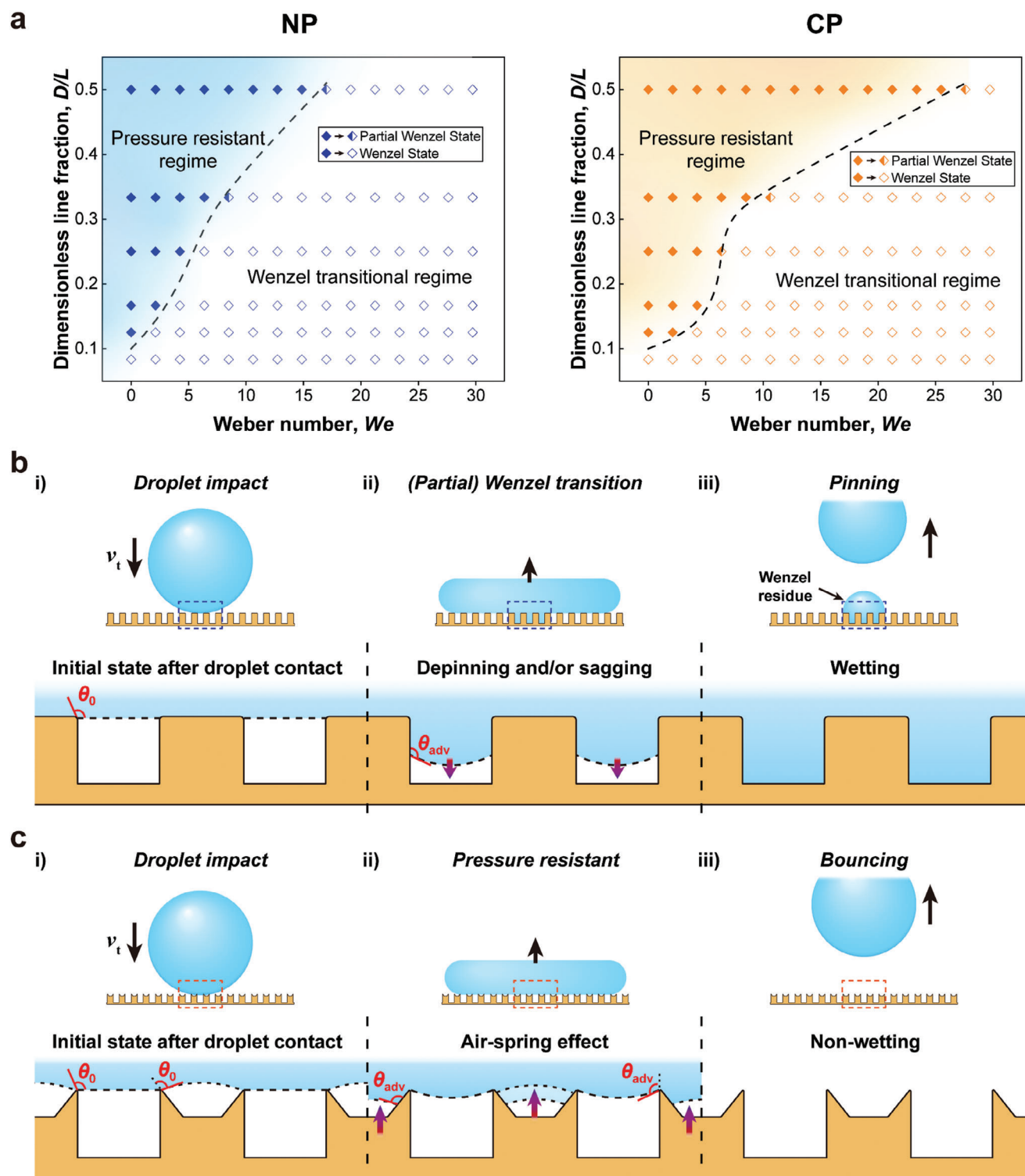


Figure 3. Impact pressure-resistant regime of the NP and CP microstructures followed by deducing mechanisms. a) Phase maps of pressure-resistant properties along with NP and CP surfaces as a function of Weber number (We). b) Possible CWT mechanism on the NP surface by the critical v_t , We , of a water droplet. c) Deducing water droplet bouncing behavior on the CP surface with equal v_t and We for the NP surface. The scale of schematics does not concern the real-world scale.

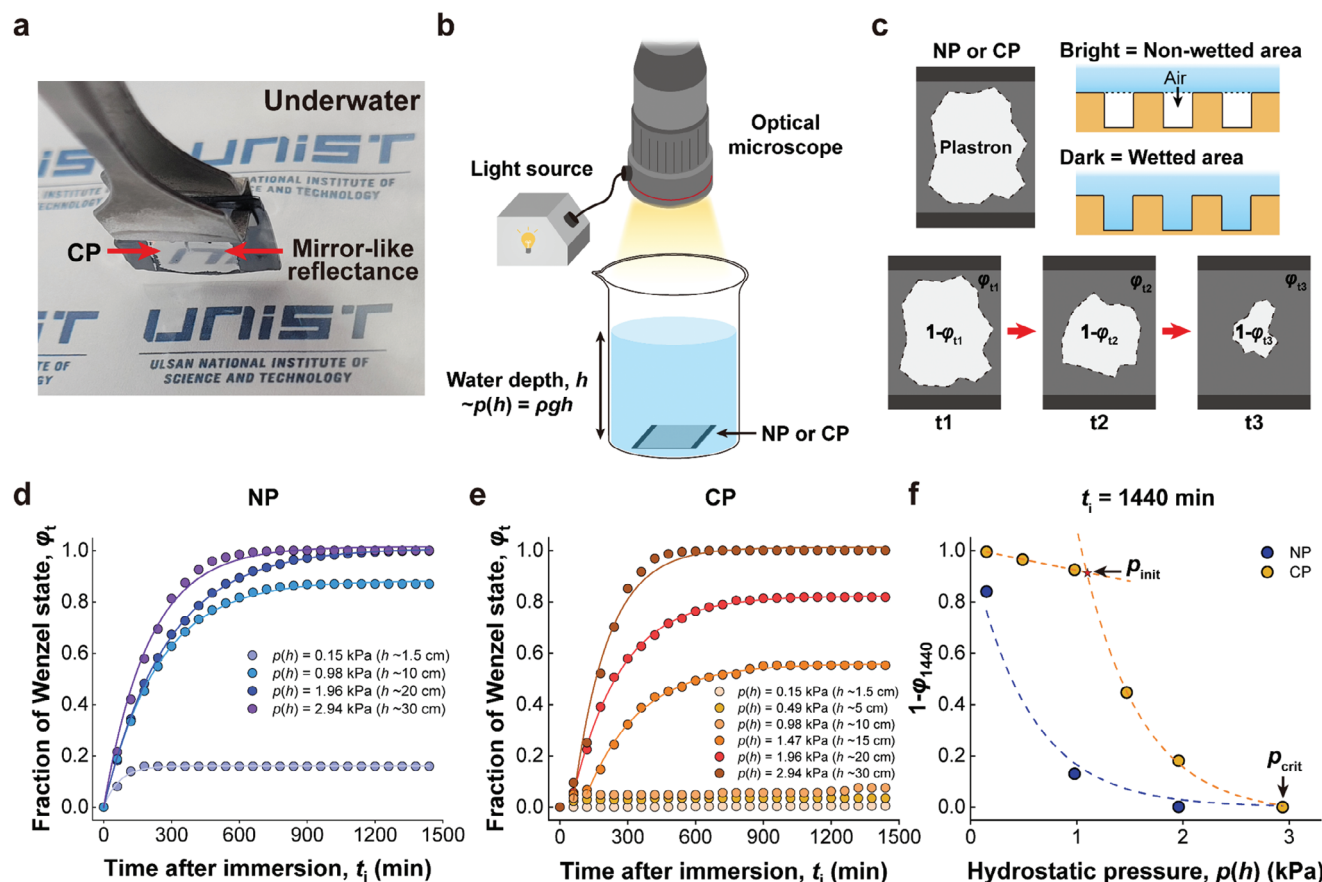


Figure 4. Superior plastron retention property of CP surface. a) Mirror-like reflectance of CP surface underwater due to the entrapped air film, plastron. Schemes as to b) experimental set-up for the investigation of underwater CWT and c) acquired snapshots regarding immersion time with a bright field for entrapped air and a dark field for the wetted area by water. The fraction of Wenzel state (ϕ_t) for the d) NP surface and the e) CP surface as a function of time after immersion (t_i) at varying hydrostatic pressure of 0.15–2.94 kPa (water depths of 1.5–30 cm). The solid lines denote fitted lines with exponential functions. f) Saturated plastron (trapped air) after 1440 min, $1 - \phi_{1440}$, for the NP and CP surfaces as a function of $p(h)$. Dashed curve lines indicate fitted lines for the NP and the CP surfaces, respectively, based on the exponential function. A dashed linear line (at lower $p(h)$) denotes a fitted line for the CP surface based on the linear function.

surface, we demonstrate the relation between effective air volume (unit air volume of the concavity/unit area) and critical We of each surface (Note S6 and Figure S18a, Supporting Information). Notably, the critical We of each surface is directly proportional to the effective air volume of the surface (Figure S18b, Supporting Information). Thus, the higher effective air volume of the CP surface would be a key parameter for designing a stable superhydrophobic surface.

Nonetheless, the CP surface may exhibit limited droplet-repellent function in specific cases. For example, if the CP surface is exposed to a water-condensing environment, due to the higher number of nucleation sites, it is expected to possess lower CWT resistance compared to NP and TCP. To point out the limitations and guide the future research direction, we examined the impact pressure resistance of the NP, CP, and TCP surfaces ($D/L = 0.5$) with the droplet We of ≈ 4.2 and ≈ 12.7 , maintaining a surface temperature of -10 °C (a supercooled surface which can enhance droplet condensation). As expected, the CP surface did not repel the $We \approx 4.2$ of water droplets possibly due to the higher number of water nucleation sites, while the other surfaces (partially) repelled the water droplets (Note S7 and Movie S6,

Supporting Information). Meanwhile, with the water droplets of $We \approx 12.7$, all the surfaces performed similar wetting behavior (further discussion in Note S7 and Movie S6, Supporting Information). Therefore, when designing water-repelling surfaces for water condensing environments, additional factors such as the number of nucleation sites should be thoroughly considered.

2.4. Exceptional Plastron Stability of CP Surface

We further scrutinized the underwater plastron stability of NP and CP surfaces. When the superhydrophobic surface is immersed in water, the surface can hold air between the protrusions on it and the air-trapping state called a plastron.^[11b] The plastron reflects a silvery sheen due to the mirror-like reflectance of thin air film (Figure 4a). The underwater plastron on superhydrophobic surfaces is often metastable. This indicates that slow or fast CWT may occur underwater depending on various factors.^[17a] More specifically, the rate of CWT primarily depends on the rate of air escaping the pores,^[17a] and the mass flux of air from pores to bulk water has been evaluated to increase exponentially in

response to the hydrostatic pressure.^[29] Therefore, the plastron stability of both NP and CP surfaces was investigated under the hydrostatic pressure $p(h)$ of 0.15–2.94 kPa (water depth of 1.5–10 cm), where $p(h) = \rho gh$, g is the gravitational acceleration, and h is water depth. Specifically, the NP and CP surfaces with the highest line fraction ($D/L = 0.5$) were employed for these investigations since the CP surface has performed effective concave effects against droplet impact.

DI water was filled in a glass tank thereafter the tank was placed in a room with a constant temperature and humidity of 18.5 ± 0.2 °C and $50 \pm 5\%$, respectively. The NP and CP surfaces were submerged in the water followed by imaging with a horizontally mounted optical camera (for $h \approx 1.5$ –10 cm) (Figure 4b) or smartphone (for $h \approx 15$ –30 cm, due to the limited focal length of the optical camera). The wetted area and non-wetted area can be distinguished by the difference in contrast since the trapped air film effectively reflects the light (Figure 4c; Figures S19 and S20, Supporting Information). We then defined a fraction of Wenzel state (ϕ_i) by dividing the wetted area with the initial plastron area on the NP/CP surfaces as a function of time-after-immersion (t_i).

Figure 4d,e represents ϕ_i of the NP and CP surfaces with immersion time, respectively, at varying $p(h)$. The higher $p(h)$ resulted in a faster CWT (Figures S19 and S20, Supporting Information) and a higher saturated ϕ_i . The ϕ_i exponentially increased with increasing immersion time following the modified simple first-order kinetic model (Note S8 and Figure S21, Supporting Information).^[17a] It is important to note that, at low $p(h)$, only a small fraction of the CP surface has gone through the CWT ($\approx 7.5\%$ at $p(h) = 0.98$ kPa; $\approx 3.5\%$ at $p(h) = 0.49$ kPa; and $\approx 0.5\%$ at $p(h) = 0.15$ kPa). Moreover, a $p(h)$ of 2.94 kPa was required for CP to achieve a complete CWT. Contrary to the CP surface, the NP surface experienced a higher fraction ($\approx 15\%$) of CWT even at small $p(h) \approx 0.15$ kPa, achieving complete CWT at $p(h) \approx 1.96$ kPa which is $\approx 33\%$ lower than the value for CP. Consequently, we found the enhanced underwater plastron (trapped air film) stability of the CP surface compared to the NP surface below the $p(h)$ of 2.94 kPa.

All the surfaces at each $p(h)$ show saturated ϕ_i after $t_i = 1440$ min. Therefore, the retained final plastron volume fraction can be described as $1 - \phi_{1440}$. Assuming an ideal gas, a higher $p(h)$ results in a higher fugacity (diffusion) of air in the water. The fugacity can be substituted by an equilibrium partial pressure, p' . As a result, the correlation between the p' and the $p(h)$ can be termed as:^[29b]

$$\ln\left(\frac{p'}{p'_0}\right) = \frac{v_m}{RT} [p(h)] \quad (2)$$

v_m is a partial molar volume of gas (assumed as constant),^[29a] R is the gas constant, T is temperature, and $p'_0 \approx 1$ is an initial equilibrium partial pressure. In our system, the plastron volume is considered constant so, the variation in pressure from the initial state is inversely proportional to the volume change. Therefore, the final plastron volume fraction, $1 - \phi_{1440}$, can be approximated as:

$$(1 - \phi_{1440}) \sim e^{-\frac{v_m}{RT} [p(h)]} \quad (3)$$

where $\frac{v_m}{RT}$ is believed constant, describing an exponential decrease in $1 - \phi_{1440}$ with increasing $p(h)$ ($p(h)$ is constant for here because the change of h from evaporation is negligible with < 0.1 mm for 1.5 cm and < 1 mm for other heights). Indeed, the exponential decay of $1 - \phi_{1440}$ (plastron) for the NP regarding $p(h)$ was observed, which means the metastable underwater stability of the NP surface even at a low $p(h) \approx 0.15$ kPa (Figure 4f). In contrast, a high fraction of retained plastron ($\approx 92.5\%$) was observed on the CP surface up to the $p(h) \approx 0.98$ kPa with a linear relationship between $1 - \phi_{1440}$ and $p(h)$. Above that pressure, the CP surface seemed to go through an exponential decay of the plastron volume fraction ($1 - \phi_{1440}$) at a higher $p(h)$, inferring there's an initial hydrostatic pressure, p_{init} , for activating the CWT of the CP surface (Figure 4f). Therefore, the retaining plastron volume fraction ($1 - \phi_{1440}$) in the CP surface can be approximated as:

$$(1 - \phi_{1440}) \sim e^{-\frac{v_m}{RT} [p(h) - p_{init}]} \quad (4)$$

Since the $\frac{v_m}{RT}$ is equal to that of the NP surface, the p_{init} for the CP surface is acquired as ≈ 1.07 kPa based on the plots in Figure 4f. Concerning the concave structure of the CP surface, a convex air cap could be formed on the concave part underwater, pressing with downward Laplace pressure, ΔP_L (Figure S22, Supporting Information). The $p_{init} \approx 1.07$ kPa is quite similar to the possible $\Delta P_L \approx 1.17$ kPa (minimum value in Note S9, Supporting Information), implying the ΔP_L on the concave cavities could be determined as a p_{init} for the CP surface. Moreover, the CP surface experienced an NP-like complete CWT at $p(h) \approx 2.94$ kPa, where $p(h) \approx 2.94$ kPa can be considered as a critical hydrostatic pressure, p_{crit} , for the NP-like wetting behavior of the CP surface.

In detail, we can distinguish the underwater wetting state of the CP surface into 3 regimes as a function of the $p(h)$: i) non-wetting state ($p(h) < p_{init}$), ii) intermediate state ($p_{init} < p(h) < p_{crit}$), and iii) NP-like wetting state ($p(h) \geq p_{crit}$). i) Below the $p(h)$ of p_{init} , there exists a rapid drop of plastron volume fraction (within ≈ 120 min), followed by a stable partial Cassie-Baxter state with a very low CWT fraction. The fraction of CWT increases gradually with increasing $p(h)$, which may be due to some heterogeneity in CPs. ii) The case between $p_{init} \approx 1.07$ kPa and $p_{crit} \approx 2.94$ kPa can be defined as an intermediate (transitional) state due to the similar magnitude of ΔP_L and $p(h)$. As the air diffusion occurs from the convex air cap, the volume of the air cap will be reduced followed by the decrease in curvature radii of the air cap. The smaller radii lead to a higher ΔP_L than the initial $\Delta P_L \approx 1.17$ kPa (Note S9, Supporting Information). Therefore, the competition of $p(h)$ and increasing ΔP_L leads to an intermediate wetting state of the CP surface under the $p(h)$ from $p_{init} \approx 1.07$ kPa to $p_{crit} \approx 2.94$ kPa. iii) Above the $p_{crit} \approx 2.94$ kPa, the CP loses its concave characteristic and acts similarly to the NP surface in terms of the CWT. This indicates that high $p(h)$ has triggered the instantaneous filling of concave regions of the pillars. In this regard, adjusting the p_{init} induced by the concave cavities would be critical for outstanding plastron stability underwater.

2.5. Concave Effect for Underwater Plastron Stability

We introduced fluorescence confocal microscopy to certify the formation of convex air caps on the concave structures. The CP

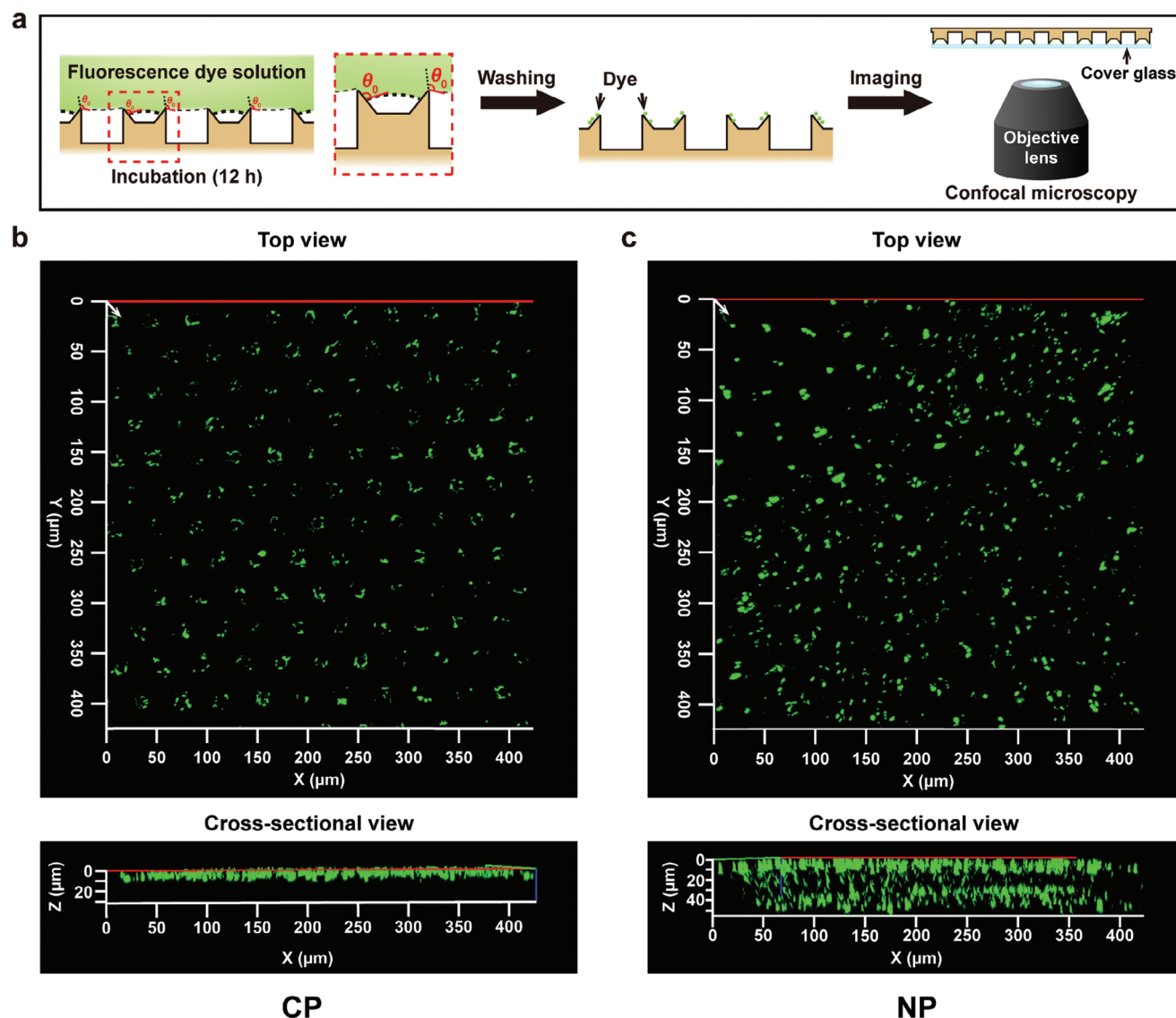


Figure 5. Fluorescence confocal microscopy images of the NP and CP surfaces after immersion. a) Schematics for experimental method. Imaging was conducted after immersion of the surfaces in the fluorescent dye solution. Z-stacked images for b) NP surface and c) CP surface, detecting adhered dyes after immersion. Images of a whole range from the top to the bottom surfaces were stacked.

and NP surfaces were immersed in a 1.5 cm depth of fluorescent dye solution (surface tension of $74.1 \pm 0.4 \text{ mN m}^{-1}$) (Note S10 and Figure S23, Supporting Information) for 720 min followed by washing and blowing. The adhered dyes on the CP and NP surfaces were then imaged using an inverted confocal microscope stacking in a z-direction from the top to the bottom surface (Figure 5; and Figure S24, Supporting Information). We imaged particularly the wetted area of the NP surface (fraction of Wenzel state) to investigate whether the dark area in Figure S19 (Supporting Information) is genuinely in the Wenzel state or not. Conversely, we could not find any portion of the Wenzel state when imaging the CP surface. We found a trace of dyes only at the bottom edge of the concave cavities, not their center (Figure 5b; and Figure S24a, Supporting Information). Besides, there were no dyes on the bottom of the CP structures implying a stable Cassie-

Baxter state during immersion (Figure S24a, Supporting Information). This illustrates the air/water interfaces above the concave parts didn't bulge into the structure, not touching the inner center of concave cavities. For that reason, the ΔP_L from the convex air caps would compete with $p(h)$ on the air/water interfaces between pillars. Existing higher pressure (ΔP_L) than $p(h)$ might lead to an inhibition of air diffusion through the air/water interfaces between pillars owing to the favorable mass flux of air under higher pressure (Figure S22, Supporting Information). On the contrary, some portion of the NP surface, both the top and bottom of the structure, was imaged with adhered dyes indicating the CWT on the NP surface (Figure 5c; and Figure S24b, Supporting Information). To advocate our demonstration, a bubble rupture time for both NP and CP surfaces was measured (Note S11 and Figures S25 and S26, and Movie S7, Supporting Information).

Collectively, these comprehensive results offer evidence that the concave effect forming convex air caps on the cavities is key to the stable Cassie-Baxter state of the CP surface.

3. Conclusion

In summary, we unveil the biomimetic concave effect for a stable superhydrophobicity under impact and hydrostatic pressure. The dynamic behavior of falling water droplets on the fabricated concave pillar (CP) surfaces ($D/L = 0.125\text{--}0.5$) was investigated by comparing them to the same D/L of standard superhydrophobic normal pillar (NP) surfaces. Within the critical v_t at which the NP surfaces encountered the partial or complete CWT, the CP surfaces appeared the enhanced impact pressure resistance together with bouncing droplets or only a partial CWT. Furthermore, the wetting phase diagram showed that the CP surface was much more stable under the impact pressure, maintaining the Cassie-Baxter state up to a larger We (≈ 27.6 at $D/L = 0.5$) compared to that of the NP surface (≈ 17.0 at $D/L = 0.5$). Next, the underwater plastron stability of the NP and CP surfaces with $D/L \approx 0.5$ was studied at varying hydrostatic pressures ($p(h)$). As we expected, the CP surface withstood higher hydrostatic pressure reaching a complete CWT at $p(h) \approx 2.94$ kPa, whereas the NP surface easily released its trapped air film and became Wenzel state even at $p(h) \approx 1.96$ kPa. The results from fluorescence confocal microscopy supported that the convex air caps are constructed on the concave structures applying higher ΔP_L than certain $p(h)$. Given that the ΔP_L would favor the air diffusion through the air cap on the concavity, opposing the $p(h)$ on the air/water interfaces between pillars. As a result, the CP surface seems to prevent the underwater CWT resulting from the favorable air diffusion on the concavity. Therefore, we identified the competing pressure owing to the concave effect could be attributed to the stable underwater wetting stability and superhydrophobicity. Our demonstrations of the concave effect countering the impact and hydrostatic pressure can offer a design concept for other superhydrophobic surfaces with a stable Cassie-Baxter state, further advancing in-depth explorations and state-of-the-art applications.

4. Experimental Section

Preparation of Microstructures: A 1 μm thick SiO_2 layer was thermally grown on a P-type 4-inch (100) silicon wafer (i-Nexus, Inc.) in a furnace (KHD-306, KSM). Before fabrication, the SiO_2/Si wafer was cleaned with a piranha solution (a 3:1 volume ratio of sulfuric acid, and 30% hydrogen peroxide solution) for 30 min at 80 $^\circ\text{C}$. Subsequently, the wafer was rinsed with DI water (18.2 M Ω , Milli-Q) followed by N_2 blowing. An etching mask for the SiO_2 layer was then patterned using a PR (DPR-i1549, Dongjin Semichem Co., Ltd.) by photolithography (MA/BA6-8, SÜSS MicroTec). A Cr mask divided into several patterns with hexagonal arrayed circles was used, varying D/L , for photolithography. Utilizing the dielectric inductively coupled plasma reactive ion etching system (FABstar, TTL) the 1 μm SiO_2 was vertically etched along the pattern, and the patterned SiO_2 was utilized as an etching mask for silicon. To manufacture an inverted pyramidal shape on the silicon surface, the wafer was wet etched in 5 M KOH + IPA (80:20 volume ratio) solution for 10 min at 70 $^\circ\text{C}$. The time of 10 min was set to minimize the undercut of silicon underneath the SiO_2 layer. After washing, a 0.3 μm thickness of Cr was deposited on the entire surfaces employing a DC sputter (SRN-120, SORONA) operated at 700 W power, and Cr was introduced as a protective mask for the concave parts

in the process of silicon etching. SiO_2 was etched in BOE for 10 min, also lifting off the Cr film on the SiO_2 layer. Consecutively, the revealed silicon surface was etched using a deep reactive ion etching system (Tegal 200, Tegal France) with the Bosch process (The process condition is presented in Table S1, Supporting Information). After that, Cr on the concave cavities was removed in chromium etchant (Sigma-Aldrich). To remove the nanograsses created during the process,^[30] the surfaces were immersed in pure ethanol ($\geq 99.5\%$, Sigma-Aldrich) followed by gentle sonication for 1 min. Finally, after 3 min of air plasma treatment (100 W power and flow of 30 ccm), the 1H,1H,2H,2H-Perfluorooctyl trichlorosilane (FOTS, Sigma-Aldrich) was deposited on the surface using a SAM-coater (AVC-150, SORONA). The fabrication of NP and TCP surfaces is depicted in Notes S1 and S4 (Supporting Information), respectively.

Surface Characterization: The leaf beetle was dried using a critical point dryer. The microscopic view of puvilli on the leaf beetle feet was obtained using a SEM (JSM-6390LV, JEOL) operating at 20 kV acceleration voltage after Pt coating by ion sputter (108 Auto Sputter Coater, Cressington). The morphology of fabricated microstructures was characterized using a Quanta 200 FEG SEM (FEI) with a 15 kV acceleration voltage. The wettability of surfaces was determined using a goniometer (DSA100, KRÜSS GmbH). Static contact angle was measured with ≈ 6 μL of DI water (18.2 M Ω , Milli-Q) on the five different points. The advancing and receding contact angles were defined by measuring a contact angle when the contact line shifted during expanding and shrinking of 0–10 μL droplet with the rate of 0.37 $\mu\text{L s}^{-1}$. The intrinsic contact angle of the flat FOTS surface was measured with the non-patterned parts of the fabricated surface. The hydrophilic fumed silica (AEROSIL 380, Evonik Industries AG) was used and roughly spread on the CP surface ($D/L = 0.5$) to evaluate the self-cleaning property of the CP surface. The CP surface was attached to the slide glass using double-sided tape and then positioned with a hinge angle of $\approx 30^\circ$. Afterward, the DI water droplets were continuously dosed and rolled on the contaminated surface.

Droplet Impact Dynamics Analysis: Dynamic behaviors of water droplets were investigated using a high-speed camera (Fastcam Mini UX50, Photron), recording at a frame rate of 2500 fps. Additionally, the l_0 was measured using a pixel-to-length calibration in connected software for the high-speed camera (PFV, Photron). Using a syringe pump (NE-300, New Era) with 10 $\mu\text{L min}^{-1}$ pumping, ≈ 2 μL ($d_0 \approx 1.56$ mm) water droplets were dropped on each surface after natural detachment from a 38 G needle. The heights of the needle from the surface were 0.5–9.0 cm, and the Weber number (We) was calculated according to the terminal impact velocity, v_t . The v_t , at the instantaneous contact of a droplet to the surface, was simply computed from $v_t = \sqrt{2gH}$, where H is the initial height of droplet before departure, assuming there's negligible air resistance to droplets. The water droplets were dropped at least 3 times on each surface, and all the surfaces experienced CWT behaviors at the same We range. Additionally, all investigations were implemented at room temperature of 23 $^\circ\text{C}$. The details of impacting droplets on the supercooled surfaces are described in Note S7 (Supporting Information).

Characterization of Underwater Wetting Behavior: The underwater wetting behaviors for both NP and CP surfaces were investigated in the room with constant temperature (18.5 ± 0.2 $^\circ\text{C}$) and humidity ($50 \pm 5\%$). Glass tanks were filled with ultrapure DI water (18.2 M Ω , Milli-Q) then equilibrated to the adjusted room temperature. The temperature of the water was monitored using a temperature probe (SS200) supporting a hot plate. Before each submersion, the FOTS were redeposited after surface cleaning (with air plasma and piranha solution), then stored the surface in the analyzing room overnight. Afterward, the surfaces were solely and gently submerged to the bottom of the water from the top water surface, and the position of the surfaces was adjusted for imaging; usually took 30 seconds for adjustment. Subsequently, for the water depths of 1.5–10 cm, the snapshots of the surfaces were captured every 60 min during 1440 min of immersion using the above-mentioned high-speed camera. For 15–30 cm depths, a smartphone (SM-N960N, Samsung) was employed for recording. Also, the snapshots were pictured at fixed magnification for each experiment. To define the wetted area, the pixels of the bright-field area and the dark-field area were counted using Adobe Photoshop software. The bright-field area appeared due to the light reflectance of the air layer and

turned dark when the air dissipated from that area. The wetting ratio φ_t was calculated with a turned dark-field area divided into the initial bright-field area. The initial bright-field area was obtained by subtracting the initially wetted area (at $t_i = 0$) from the entire NP or CP area, and the wetted area at first was caused by defective area on the surfaces (damaged pillars). The macroscopic view of the surfaces during immersion was captured, and the total pixels of the area were counted without considering a portion of the pillar area.

Bubble Rupture Time Measurements: Underwater air dynamics were assessed in a room of constant temperature and humidity using the high-speed camera with a frame rate of 5000 fps. DI water (18.2 M Ω , Milli-Q) was filled in a custom-made liquid cell and a 1 mL syringe with a 38 G needle was fixed through the hole at the bottom of the cell. The surfaces were reversely mounted at a depth of 1 cm and equilibrated for 1 min. Using the syringe pump with a pumping rate of 10 $\mu\text{L min}^{-1}$, the bubbles (≈ 1 mm diameter) were dispensed at ca. 2.5 mm below the surface from the 38 G needle after natural departure. The bubble rupture time (t_r) was defined as a time from $t = 0$ to right before rupture, and $t = 0$ was considered as a moment when bubbles stopped bouncing. Ten measurements of bubble rupture time were measured and averaged for each surface.

Supporting Information

Supporting Information is available from the Wiley Online Library or from the author.

Acknowledgements

J.L. and J.P. contributed equally to this work. This research was supported by the Basic Science Research Program (NRF-2023R1A2C2004762) and the Nano & Material Technology Development Program (RS-2024-00408845) through the National Research Foundation of Korea (NRF) grant funded by the Ministry of Science and ICT. This study contains the results obtained at UNIST Central Research Facilities (UCRF).

Conflict of Interest

The authors declare no conflict of interest.

Data Availability Statement

The data that support the findings of this study are available from the corresponding author upon reasonable request.

Keywords

concave pillar, Laplace pressure, plastron, superhydrophobic, Weber number

Received: July 1, 2024
Revised: September 10, 2024
Published online:

- [1] T. Young, *Philos. Trans. R. Soc. London* **1805**, 95, 65.
- [2] a) R. N. Wenzel, *Ind. Eng. Chem.* **1936**, 28, 988; b) A. B. D. Cassie, S. Baxter, *Trans. Faraday Soc.* **1944**, 40, 546.
- [3] N. A. Patankar, *Langmuir* **2003**, 19, 1249.
- [4] a) Y. Lu, S. Sathasivam, J. Song, C. R. Crick, C. J. Carmalt, I. P. Parkin, *Science* **2015**, 347, 1132; b) F. Geyer, M. D'Acunzi, A. Sharifi-Aghili, A. Saal, N. Gao, A. Kaltbeitzel, T.-F. Slood, R. Berger, H.-J. Butt, D. Vollmer, *Sci. Adv.* **2020**, 6, eaaw9727; c) L. Zhang, A. G. Zhou, B. R. Sun, K. S. Chen, H.-Z. Yu, *Nat. Commun.* **2021**, 12, 982.
- [5] a) Y. Hou, M. Yu, Y. Shang, P. Zhou, R. Song, X. Xu, X. Chen, Z. Wang, S. Yao, *Phys. Rev. Lett.* **2018**, 120, 075902; b) M. Zhou, L. Zhang, L. Zhong, M. Chen, L. Zhu, T. Zhang, X. Han, Y. Hou, Y. Zheng, *Adv. Mater.* **2024**, 36, 2305322.
- [6] a) Q. Sun, D. Wang, Y. Li, J. Zhang, S. Ye, J. Cui, L. Chen, Z. Wang, H.-J. Butt, D. Vollmer, X. Deng, *Nat. Mater.* **2019**, 18, 936; b) C. Yang, Q. Zeng, J. Huang, Z. Guo, *Adv. Colloid Interface Sci.* **2022**, 306, 102724; c) C. Son, Z. Yang, S. Kim, P. M. Ferreira, J. Feng, S. Kim, *ACS Nano* **2023**, 17, 23702; d) X. Zhang, S. Ben, Z. Zhao, Y. Ning, Q. Li, Z. Long, C. Yu, K. Liu, L. Jiang, *Adv. Funct. Mater.* **2023**, 33, 2212217.
- [7] a) A. B. Tesler, P. Kim, S. Kolle, C. Howell, O. Ahanotu, J. Aizenberg, *Nat. Commun.* **2015**, 6, 8649; b) S. Wooh, N. Encinas, D. Vollmer, H.-J. Butt, *Adv. Mater.* **2017**, 29, 1604637; c) T. P. Rasitha, S. Sofia, B. Anandkumar, J. Philip, *Colloids Surf., A* **2022**, 647, 129194; d) W. Gu, W. Li, Y. Zhang, Y. Xia, Q. Wang, W. Wang, P. Liu, X. Yu, H. He, C. Liang, Y. Ban, C. Mi, S. Yang, W. Liu, M. Cui, X. Deng, Z. Wang, Y. Zhang, *Nat. Commun.* **2023**, 14, 5953.
- [8] a) D. Wakerley, S. Lamaison, F. Ozanam, N. Menguy, D. Mercier, P. Marcus, M. Fontecave, V. Mougél, *Nat. Mater.* **2019**, 18, 1222; b) J. Zhang, B. Zhao, W. Liang, G. Zhou, Z. Liang, Y. Wang, J. Qu, Y. Sun, L. Jiang, *Adv. Sci.* **2020**, 7, 2002630; c) K. Li, S. Zou, J. Zhang, Y. Huang, L. He, X. Feng, *ACS Catal.* **2023**, 13, 9346; d) L. Cui, B. Chen, L. Zhang, C. He, C. Shu, H. Kang, J. Qiu, W. Jing, K. Ostrikov, Z. Zhang, *Energy Environ. Sci.* **2024**, 17, 655; e) M. Sun, J. Cheng, M. Yamauchi, *Nat. Commun.* **2024**, 15, 491.
- [9] a) B.-J. Ju, J.-H. Oh, C. Yun, C. H. Park, *RSC Adv.* **2018**, 8, 28825; b) K. Chen, Y. Li, G. Yang, S. Hu, Z. Shi, G. Yang, *Adv. Funct. Mater.* **2023**, 33, 2304809; c) S. Jung, S. Woo, D. Heo, S. Park, S. Cho, M. Choi, Y. Cho, S. Lee, J. Hong, *Chem. Eng. J.* **2023**, 457, 141066; d) B. Zhang, W. Xu, L. Peng, Y. Li, W. Zhang, Z. Wang, *Nat. Rev. Electr. Eng.* **2024**, 1, 218.
- [10] L. Li, J. Wei, J. Zhang, B. Li, Y. Yang, J. Zhang, *Sci. Adv.* **2023**, 9, ead1554.
- [11] a) W. Zhang, D. Wang, Z. Sun, J. Song, X. Deng, *Chem. Soc. Rev.* **2021**, 50, 4031; b) A. B. Tesler, S. Kolle, L. H. Prado, I. Thievensen, D. Böhlinger, M. Backholm, B. Karunakaran, H. A. Nurmi, M. Latikka, L. Fischer, S. Stafslien, Z. M. Cenev, J. V. I. Timonen, M. Bruns, A. Mazare, U. Lohbauer, S. Virtanen, B. Fabry, P. Schmuki, R. H. A. Ras, J. Aizenberg, W. H. Goldmann, *Nat. Mater.* **2023**, 22, 1548.
- [12] a) G. E. Fogg, *Nature* **1944**, 154, 515; b) A. B. D. Cassie, S. Baxter, *Nature* **1945**, 155, 21; c) J. A. N. Dyck, *Zool. Scr.* **1985**, 14, 137; d) M. Liu, S. Wang, L. Jiang, *Nat. Rev. Mater.* **2017**, 2, 17036.
- [13] a) M. R. Flynn, J. W. M. Bush, *J. Fluid Mech.* **2008**, 608, 275; b) W. Barthlott, T. Schimmel, S. Wiersch, K. Koch, M. Brede, M. Barczewski, S. Walheim, A. Weis, A. Kaltenmaier, A. Leder, H. F. Bohn, *Adv. Mater.* **2010**, 22, 2325; c) R. S. Seymour, P. G. D. Matthews, *J. Exp. Biol.* **2013**, 216, 164.
- [14] a) A. K. Dickerson, P. G. Shankles, D. L. Hu, *Phys. Fluids* **2014**, 26, 027104; b) S. Kim, Z. Wu, E. Esmaili, J. J. Dombroskie, S. Jung, *Proc. Natl. Acad. Sci. USA* **2020**, 117, 13901; c) L. Wang, R. Wang, J. Wang, T.-S. Wong, *Sci. Adv.* **2020**, 6, eabb2307; d) W. Konrad, A. Roth-Nebelsick, B. Kessel, T. Miranda, M. Ebner, R. Schott, J. H. Nebelsick, *J. R. Soc., Interface* **2021**, 18, 20210676; e) D. A. Watson, M. R. Thornton, H. A. Khan, R. C. Diamco, D. Yilmaz-Aydin, A. K. Dickerson, *Proc. Natl. Acad. Sci. USA* **2024**, 121, 2315667121.
- [15] S. Wang, K. Liu, X. Yao, L. Jiang, *Chem. Rev.* **2015**, 115, 8230.
- [16] N. A. Patankar, *Langmuir* **2004**, 20, 8209.
- [17] a) D. Seo, A. M. Schrader, S.-Y. Chen, Y. Kaufman, T. R. Cristiani, S. H. Page, P. H. Koenig, Y. Gizaw, D. W. Lee, J. N. Israelachvili, *Proc. Natl. Acad. Sci. USA* **2018**, 115, 8070; b) D. Liao, M. He, H. Qiu, *Int. J. Heat Mass Transfer* **2019**, 133, 341.
- [18] a) A. Tuteja, W. Choi, M. Ma, J. M. Mabry, S. A. Mazzella, G. C. Rutledge, G. H. McKinley, R. E. Cohen, *Science* **2007**, 318, 1618; b) E. M. Domingues, S. Arunachalam, J. Nauruzbayeva, H. Mishra, *Nat. Commun.* **2018**, 9, 3606.

- [19] a) N. A. Patankar, *Langmuir* **2004**, *20*, 7097; b) R. David, A. W. Neumann, *Colloids Surf., A* **2013**, *425*, 51; c) Y. Kaufman, S.-Y. Chen, H. Mishra, A. M. Schrader, D. W. Lee, S. Das, S. H. Donaldson Jr., J. N. Israelachvili, *J. Phys. Chem. C* **2017**, *121*, 5642; d) P. Xu, J. R. Bai, P. Zhou, L. L. Wang, X. N. Sun, L. Wei, Q. F. Zhou, *RSC Adv.* **2022**, *12*, 2701.
- [20] a) S. Moulinet, D. Bartolo, *Eur. Phys. J. E.* **2007**, *24*, 251; b) N. A. Patankar, *Langmuir* **2010**, *26*, 8941; c) S. Dash, M. T. Alt, S. V. Garimella, *Langmuir* **2012**, *28*, 9606.
- [21] T.-S. Wong, C.-M. Ho, *Langmuir* **2009**, *25*, 12851.
- [22] T. Maitra, M. K. Tiwari, C. Antonini, P. Schoch, S. Jung, P. Eberle, D. Poulikakos, *Nano Lett.* **2014**, *14*, 172.
- [23] a) R. Hensel, R. Helbig, S. Aland, A. Voigt, C. Neinhuis, C. Werner, *NPG Asia Mater.* **2013**, *5*, e37; b) J. Nickerl, R. Helbig, H.-J. Schulz, C. Werner, C. Neinhuis, *Zoomorphology* **2013**, *132*, 183; c) K. Gloyna, T. Thieme, S. Gorb, D. Voigt, *Eur. J. Environ. Sci.* **2014**, *4*, 97.
- [24] M. J. Orchard, M. Kohonen, S. Humphries, *J. Exp. Biol.* **2012**, *215*, 279.
- [25] Y. Jiang, G. Liu, J. Zhou, *J. Micromech. Microeng.* **2009**, *19*, 015005.
- [26] M. A. Blauw, G. Craciun, W. G. Sloof, P. J. French, E. van der Drift, *J. Vac. Sci. Technol., B: Microelectron. Nanometer Struct.–Process., Meas., Phenom.* **2002**, *20*, 3106.
- [27] T. Deng, K. K. Varanasi, M. Hsu, N. Bhate, C. Keimel, J. Stein, M. Blohm, *Appl. Phys. Lett.* **2009**, *94*, 133109.
- [28] a) H.-M. Kwon, A. T. Paxson, K. K. Varanasi, N. A. Patankar, *Phys. Rev. Lett.* **2011**, *106*, 036102; b) C. Guo, L. Liu, R. Yang, J. Lu, S. Liu, *Langmuir* **2023**, *39*, 10199.
- [29] a) T. Enns, P. F. Scholander, E. D. Bradstreet, *J. Phys. Chem.* **1965**, *69*, 389; b) R. Poetes, K. Holtzmann, K. Franze, U. Steiner, *Phys. Rev. Lett.* **2010**, *105*, 166104.
- [30] Z. Huang, N. Geyer, P. Werner, J. de Boor, U. Gösele, *Adv. Mater.* **2011**, *23*, 285.